Divertor closure effects on the TCV boundary plasma

O. Février[a], H. Reimerdes[a], C. Theiler[a], D. Brida[b], C. Colandrea[a], B. P. Duval[a], H. De Oliveira[a], D. Galassi[a], S. Gorno[a], S. Henderson[c], M. Komm[e], B. Labit[a], B. Linehan[d], L. Martinelli[a], A. Perek[f], H. Raj[a], U. Sheikh[a], C. K. Tsui[g], M. Wensing[a], the TCV Team[1], the EUROfusion MST1 Team[2]

[a] *École Polytechnique Fédérale de Lausanne (EPFL), Swiss Plasma Center (SPC), CH-1015 Lausanne, Switzerland.*
[b] *Max-Planck-Institut fur Plasmaphysik, 85748 Garching b. Munchen, Germany.*
[c] *Culham Sci Ctr, CCFE, Abingdon OX14 3DB, Oxon, United Kingdom of Great Britain and Northern Ireland.*
[d] *Plasma Science and Fusion Center MIT, Cambridge, Massachusetts 02139, USA.*
[e] *Institute of Plasma Physics of the CAS, Za Slovankou 3, 182 00 Prague 8, Czech Republic.*
[f] *DIFFER, De Zaale 20, 5612 AJ Eindhoven, The Netherlands.*
[g] *Center for Energy Research (CER), University of California-San Diego (UCSD), La Jolla, California 92093, USA.*

Abstract

The Tokamak à Configuration Variable (TCV) has recently been equipped with gas baffles to increase its divertor closure for a broad range of divertor magnetic geometries. First experimental results reported in [1] demonstrated compatibility with a broad range of divertor magnetic geometries and confirmed the main design constraints of the baffles, in particular an increased divertor neutral pressure. The present article presents a more in-depths analysis and extended experiments of this first baffle assessment on the TCV boundary plasma. It is shown that the divertor neutral pressure increased following the installation of the baffles, as predicted by SOLPS-ITER and SolEdge2D-EIRENE simulations. Varying the divertor closure by changing the position of the plasma showed that the plasma equilibrium designed to assess the baffle effect was not far from the optimal trade-off between plasma plugging and recycling on the baffles. The baffles facilitate access to a partially detached regime in both L- and H-modes. In L-Mode, with the ion ∇B-drift directed from the X-Point to the plasma core, a reduction of the line-averaged density detachment threshold by approximately 20% is observed at the outer target, while inner strike point detachment is only achieved in the presence of baffles. Multispectral imaging shows that the CIII front moves from the outer target towards the X-Point at a lower line-averaged plasma density, indicating a colder outer leg. In H-mode, the CIII front is generally located near the X-Point between the ELMs, while without baffles, N_2-seeding is required to move the front up to that location.

Keywords: Divertor, tokamak, gas baffle

1. Introduction

Power exhaust is one of the main challenges for fusion reactors. Future reactors will likely have to operate in H-Mode, thus requiring a high power-level crossing the separatrix. Such high power, associated with a narrow Scrape-off Layer (SOL) width [2], may result in divertor target power load above the material limits in steady-state conditions. In particular, in the absence of mitigation, the target heat fluxes expected in ITER and DEMO are well above these limitations [3, 4]. Operation in the detached divertor regime is therefore foreseen as necessary to keep divertor heat fluxes in a fusion power plant within engineering limits [5, 6]. In this regime, most of the plasma exhaust heat is dissipated by radiation and plasma-neutral interaction, and at the same time the plasma pressure along the field lines in the SOL develops strong gradients providing access to low target temperatures (below 5 eV) and low particle fluxes at the targets [5]. Access to detachment is promoted by high divertor neutral pressure [5], which increases plasma-neutrals interactions and thus the transfer of energy and momentum from the plasma to neutral particles and photons. High neutral pressure in the divertor also increases the throughput of vacuum pumps, facilitates the control of the particle inventory and the helium ash removal required in a reactor. In devices with relatively closed divertors, few neutrals can escape the divertor and reach the main chamber or the core plasma, which allows for a greater neutral pressure in the divertor [7]. In addition to the material gas baffles, the plasma itself plays an important role in the containment of neutrals, through "plasma plugging". If the plasma in the divertor and at the X-point area is sufficiently dense and hot, the ionization mean free path of the neutrals becomes sufficiently small that neutrals cannot leave the divertor.

The Tokamak à Configuration Variable (TCV) [8, 9] historically features a very open divertor with a limited separation between the divertor region and the main plasma. As part of the European PEX (Plasma EXhaust) program, removable neutral baffling structures have recently been installed to allow closed divertor operation and study the impact of variable closure [10, 1]. While several divertor designs already exist to increase the divertor closure (for instance the "standard" ver-

*Corresponding author
Email address: olivier.fevrier@epfl.ch (O. Février)
[1] See the author list of S. Coda et al 2019 *Nucl. Fusion* **59** 112023.
[2] See the author list of B. Labit et al 2019 *Nucl. Fusion* **59** 086020.

tical target divertor [11, 12, 6], a tight baffling along divertor legs [13], the small-angle slot (SAS) divertors [14, 15]), one of the characteristic of TCV is its unique shaping capability, that enables the investigation of alternative configurations [16]. Therefore, a key design point of the baffling structures was the minimization of the constraints on the magnetic shaping capabilities, resulting in a baffle design featuring a large divertor chamber, compatible with configurations such as the Snowflake divertor or the Super-X. The baffle design was optimized using the SOLPS-ITER code to maximize the neutral compression ratio [10], thus offering a unique test-bench to validate the models used to design the ITER divertor.

Ref. [1] presented the first observations of the initial TCV operation with a baffled divertor. Operation with a variety of divertor configuration was demonstrated. In a reference L-Mode scenario, the increase of divertor neutral pressure with the baffles and the reduction of the detachment threshold was shown. In the present article, we discuss the first observations in greater detail and extend the analysis, in particular concerning the behavior of the divertor neutral pressure and the detachment characteristics, that are compared to observations without gas baffles and predictions from SOLPS-ITER simulations [17]. Optimization of the divertor closure is explored, and preliminary results in H-Mode are presented.

This article is organized as follows. In section 2, we present the TCV tokamak, its various diagnostics as well as the recent upgrades, in particular the installation of the divertor gas baffle to increase the divertor closure. In section 3, we discuss the main effects of the baffles in L-mode, in terms of divertor neutral pressure, target conditions and detachment onset, as well as the effect on the upstream plasma and the optimal positioning of the plasma with respect to the baffles. In part 4, first results of H-mode operation with the baffled divertor are presented and compared to non-baffled operation. Finally, in section 5, the conclusions are presented.

2. The TCV PEX upgrade

TCV [9] is a medium size tokamak with a major radius $R_0 = 0.88$ m, and $B_0 \approx 1.44$ T. Pre-upgrade and baffled TCV divertor are shown in Figure 1. A set of polycrystalline graphite baffles has been installed in the High-Field-Side (HFS) and Low-Field-Side (LFS) at $Z \approx -0.35$ m to physically separate the main chamber from the divertor chamber [10]. The selected design is compatible with alternative divertor configurations such as the Super-X or the Snowflake, Figure 1 [1]. The design of these baffles was guided by SOLPS-ITER simulations without drifts [10] in which several baffle designs were compared. The HFS baffle was kept fixed at a relatively short length, while the length of the LFS baffle was varied. It was found that the efficiency of the baffles is well characterized by the flux coordinate of the baffle tip. From these simulations, a baffle with intermediate length was selected. It constitutes a trade-off between good divertor physical closure and the need to maintain a low level of recycling on the baffle. The selected baffle further resulted in the lowest target electron temperature T_e and highest target electron density n_e, for given upstream density and input parameters. Once the final design had been established, additional SOLPS-ITER simulations (with [18] and without drifts [17]) were carried out to quantify their effect on the divertor performance, in a scenario identical to the one that will be presented in section 3.1. The simulations predicted an increase of the divertor neutral density by a factor 5, as well as an increase of the neutral compression, defined as the ratio of main chamber averaged neutral density to the average divertor neutral density, by one order of magnitude. Access to detached regime was predicted to be facilitated by the enhanced volumetric losses in the divertor. In the following section, we will experimentally test these predictions.

TCV is equipped with several gas valves for seeding and fueling and an extensive set of divertor diagnostics, Figure 1. The recently extended set of wall-embedded Langmuir Probes (LPs) [19, 20] covers the entire divertor, as well as the main chamber facing side of the baffles. A recently added Reciprocating Divertor Probe Array (RDPA) [21] features a radial array of twelve Langmuir Mach-probes that provide two-dimensional (2D) measurements across the TCV divertor plasma up to the X-point. T_e an n_e measurements are obtained from the TS diagnostic. Figure 1 also shows the ports that connect to baratron pressure gauges (labeled p_n^{div}, p_n^{45}, p_n^{tmp} and p_n^{mid}) via extension tubes. Also used in this work is the MANTIS (*Multispectral Advanced Narrowband Tokamak Imaging System*) [22, 23, 24], used to gain further information on line radiation and distribution in the divertor region. The captured images are tomographically inverted to obtain two-dimensional poloidal maps of the emissivity of the selected radiation lines. In this work, we will focus on the CIII (465 nm) emissivity. A "CIII-front" can be defined as the location where the emissivity along the outer leg has dropped by 50% [25]. In previous studies [25, 16], it was shown to be a good proxy for the location of a cold radiative region along the divertor leg. Therefore, a movement of this front towards the X-Point indicates the cooling of the divertor plasma, and, thereby, a proximity to detachment.

3. Investigation of divertor baffling in L-Mode

3.1. Reference scenario and first observations

To assess the effect of the baffles on L-mode operation, the reference scenario shown in figure 2 has been developed. It is an Ohmically heated Lower-Single-Null (LSN) plasma with a plasma current of $I_p = 250$ kA and with the ion ∇B-drift pointing up (away from the X-point) to avoid transition to H-Mode. The X-point is centered between the HFS and the LFS baffle tips. In this scenario, the feedback-controlled line-averaged density $\langle n_e \rangle$ is linearly increased using valve #1 for D_2 fueling rate and a chord of a Far-Infrared interferometer (FIR) to measure $\langle n_e \rangle$. The main metric used in [10, 17] to quantify the impact of the baffles is the neutral compression ratio c_D, defined based on the ratio between the average neutral density in the divertor and main chamber. Since neutral density is a challenging quantity to measure in the vessel volume, an experimentally simpler compression ratio can be defined by the

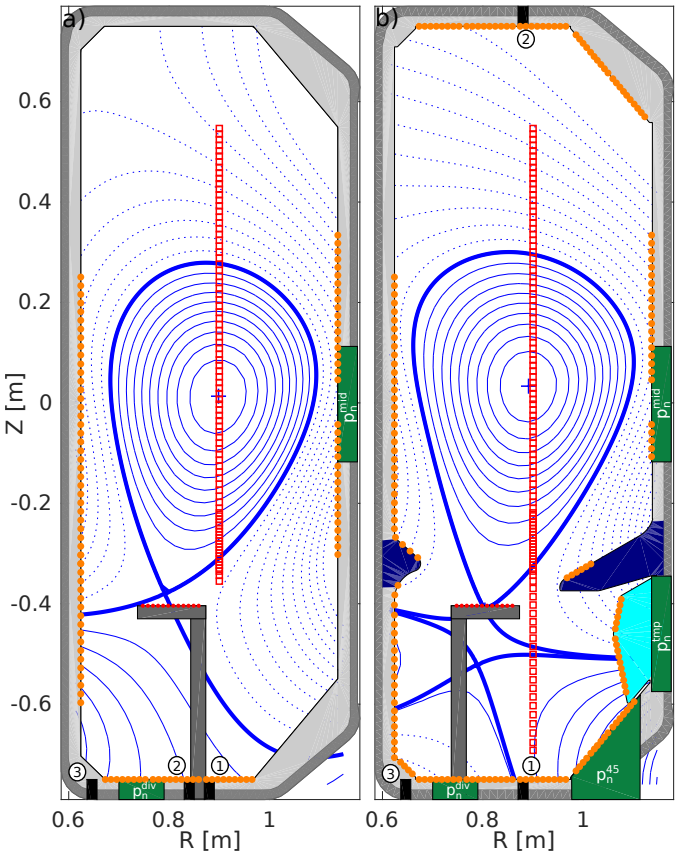

Figure 1: Panels a) (respectively b) Poloidal view of the TCV vacuum chamber before (resp. after) the installation of the divertor gas baffles (dark blue) and a *port protection tile* (cyan) [1]. The orange dots correspond to the wall Langmuir probes. The black rectangles indicate the poloidal location of the gas valves used for fueling or seeding. The circled numbers indicate the numbering of these gas valves. The L-shaped mast is the reciprocating probe RDPA, plotted here at its maximum extent. The red squares correspond to the measurements points of the Thomson Scattering (TS) system. The green rectangles show the ports onto which the pressure gauges are attached via an extension tube. Two baffle-compatible plasma equilibria (Super-X and Snowflake) are plotted.

ratio of neutral pressure measured via the midplane and divertor baratron, $c_D^{exp} = p_n^{div}/p_n^{mid}$. Unfortunately, the main chamber neutral pressure after the baffle installation falls below the sensitivity threshold of the presently installed midplane baratron [1], and c_D^{exp} cannot currently be evaluated. For this reason, we focus on the measurement of the divertor neutral pressure.

For $\langle n_e \rangle \leq 9.5 \times 10^{19}$ m^{-3}, $\langle n_e \rangle$ evolves similarly and linearly with time in all discharges, figure 2. A drastic change of behavior of $\langle n_e \rangle$ is however seen at higher $\langle n_e \rangle$ with one of the baffled cases exhibiting a sudden jump in $\langle n_e \rangle$, as already noted in [1]. The phenomenon can be seen at the same time in all vertical chords of the FIR, indicating that it is not caused by the spatial propagation of a high-density front, but a "global" phenomenon. Statistics over 11 similar discharges exhibiting the same event show that this sudden transition in the divertor regime and plasma plugging, labeled thereafter BURP (*aBrupt Unexpected Reduction of Plasma plugging*), typically occurs at $p_n^{div} = 0.06$ Pa (±10%), $\langle n_e \rangle = 9.8 \times 10^{19}$ m^{-3} (±8%). It is, however, not a general occurrence in scenarios with divertor baffles, and such phenomenon has never been observed in the absence of baffles on TCV. Following the BURP, the radiation level and the divertor neutral pressures decrease to levels typical for unbaffled reference discharge. In baffled discharges that do not undergo such a BURP, the radiation level and the divertor neutral pressure both keep increasing steadily with $\langle n_e \rangle$. A possible interpretation of the BURP is a sudden loss of divertor neutral plugging. At low density, neutrals that originates from gas puffing or recycling at the divertor targets are confined in the divertor by the combined action of the baffles and the relatively hot, ionizing plasma in between. At higher $\langle n_e \rangle$, we speculate that the X-point region plasma becomes cold enough that it cannot prevent the neutrals from entering the core and the main chamber anymore. This results in a sudden flooding of the core with neutrals, leading to a spike in density as well as a stop to the increase in p_n^{div}. Tomographic inversions of the bolometry signals show a movement of the peak radiation region, located near the X-point before the BURP, into the confined region, before going back "down" to the X-Point after the BURP, which supports the interpretation of sudden divertor neutrals and impurity release. After the BURP, the plugging of the divertor remains reduced, putting the discharge on a trajectory closer to an unbaffled case.

For $\langle n_e \rangle$ below 9.5×10^{19} m^{-3}, the radiated power is generally higher in discharges with baffles, figure 2. Tomographic inversions (not shown here) show that this is due to higher radiated power in the divertor and in the X-Point region, while the main chamber radiation in baffled and unbaffled cases remains similar. The increase of divertor radiation can be attributed to higher divertor density and lower temperature, as will be shown in section 3.3. p_n^{div}, measured in the *Private Flux Region* (PFR), reveals that the divertor neutral pressure is significantly higher in cases with baffles than without baffles. This shows that the primary purpose of the baffles, to increase the pressure in the divertor, has been achieved with the present baffle design [1]. At higher $\langle n_e \rangle$, the baffled case which does not exhibit a BURP continues to have higher divertor neutral pressures and total radiated power, although the peak radiation moves to the main chamber HFS, in a MARFE-like structure [26].

In addition to the occurrence, or not, of BURPs, some variations among different repeats of the L-mode reference discharge were also seen on other parameters. An example is the total amount of D_2 gas fuelling needed to reach a given $\langle n_e \rangle$. At high $\langle n_e \rangle$, this quantity is largest right after a boronization [27, 28] and then decreases over time. This effect is likely related to wall conditions, which are known to significantly impact the behavior of a discharge [28]. Some weak correlation was also identified with the level of residual N_2 in the machine. Variations among discharges can also be seen in the divertor neutral pressure achieved for a given $\langle n_e \rangle$, as shown in figure 3 for a series of 18 repeats of the reference baffled scenario, and 4 repeats of the unbaffled scenario. While there is significant scatter of p_n^{div} at high $\langle n_e \rangle$, the baffled cases generally feature a 2-5 times higher divertor neutral pressure, in quantitative agreement with predictions by SOLPS-ITER [17]. The absolute values of divertor neutral pressure are, however, overestimated by a factor 2-8 in the simulations. The reason for this discrepancy is currently unknown, although uncertainties in the model used for the syn-

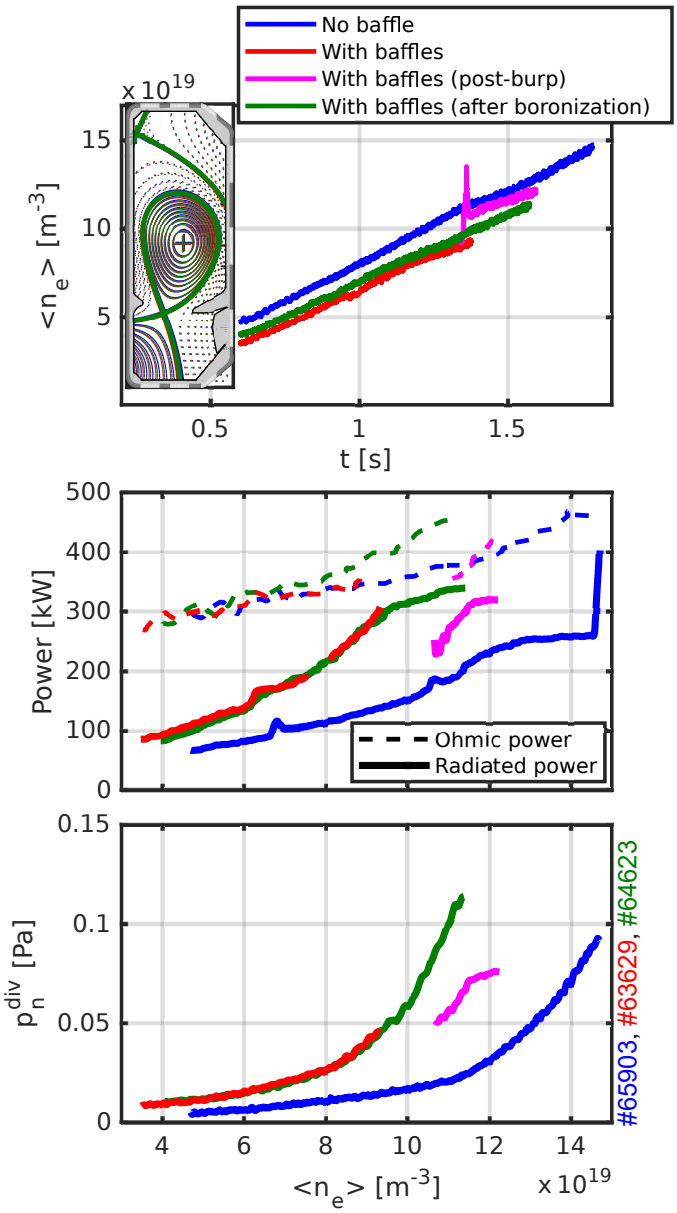

Figure 2: (a) Time evolution of the line-averaged density $\langle n_e \rangle$ in density ramp discharges without baffles (blue) and with baffles (red, magenta, and green), in the L-mode reference scenario shown in the insert at the left. (b) Evolution of the Ohmic power (dashed lines) and of the total radiated power (solid lines) for these three cases, as a function of $\langle n_e \rangle$. (c) Evolution of the divertor neutral pressure p_{div} as a function of $\langle n_e \rangle$(see figure 1 for the definition).

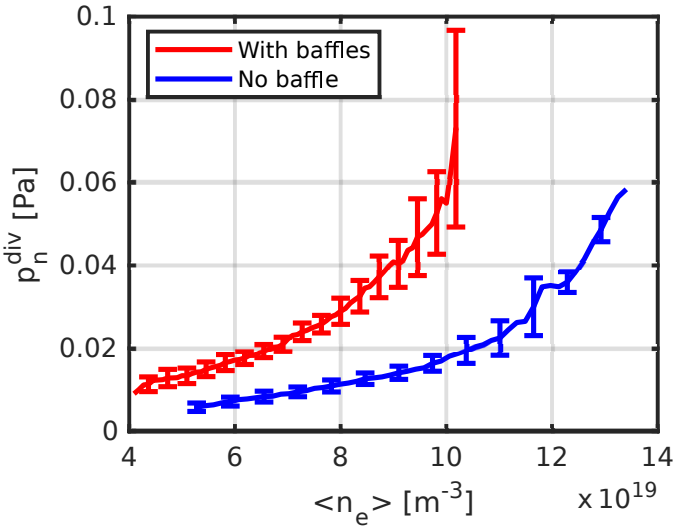

Figure 3: Average and standard deviation of the p_n^{div} as a function of the line-averaged density $\langle n_e \rangle$ for a series of 4 cases without baffle (blue), and 18 nominally identical discharges with both baffles installed (red).

thetic baratrons in the simulations could be partially responsible for the difference.

3.2. Optimizing divertor closure

The plasma equilibrium presented in the previous section was designed to have a good clearance with respect to the baffles and to be similar to the scenario used to optimize the baffles length [10]. In this section, we analyze a set of experiments to assess whether changes in the equilibrium, and therefore in the plasma plugging, can increase the effectiveness of the baffle, figure 4. The case labeled "medium" corresponds to the reference configuration discussed in section 3.1. The configurations are parametrized by the ρ_ψ value of the first flux-surface that is intercepted by the outer (resp. inner) baffle, $\rho^{lim}_{\psi,outer}$ (resp. $\rho^{lim}_{\psi,inner}$), as well as the corresponding distance to the separatrix (remapped upstream), $\mathrm{dr}^{lim}_{us,outer}$ (resp. $\mathrm{dr}^{lim}_{us,inner}$), Table 1. ρ_ψ is the normalized poloidal magnetic flux coordinate, defined as $\rho_\psi = \sqrt{(\psi - \psi_0)/(\psi_1 - \psi_0)}$ with ψ the poloidal magnetic flux and ψ_0 and ψ_1 the poloidal magnetic flux at the magnetic axis and at the primary X-point, respectively. Table 1 also reports the heat flux decay length, λ_q [2] evaluated from Infra-red measurements, averaged between $t = 0.8$ s and $t = 0.95$ s. Other discharge parameters (I_P, $\langle n_e \rangle$ ramp, fueling location) were kept constant.

Case	$\rho^{lim}_{\psi,outer}$	$\mathrm{dr}^{lim}_{us,outer}$	$\rho^{lim}_{\psi,inner}$	$\mathrm{dr}^{lim}_{us,inner}$	λ_q
Close	1.07	2.1 cm	1.07	1.87 cm	$\approx$ 2.9 mm
Medium	1.09	2.66 cm	1.08	2.36 cm	$\approx$ 2.6 mm
Far	1.11	-	1.04	1.11 cm	$\approx$ 2.8 mm

Table 1: Summary of ρ^{lim}_{ψ}, dr^{lim}_{us} and λ_q for the cases investigated in this section. In the "far" case, the limiting flux surfaces would extend beyond the plasma-facing components if mapped upstream.

The evolution of the neutral pressure as a function of $\langle n_e \rangle$ as measured by the floor baratron (p_n^{div}) and in the turbo-pump duct (p_n^{tmp}) is shown in figure 4(a,b). Due to the location of the baratron in the turbo-pump duct, which is in a pumped duct contrary to the floor baratron, the measured p_n^{tmp} is generally lower. To account for this effect, we correct p_n^{tmp} by a factor 1.5, which yields a good quantitative agreement with p_n^{div} when gas in injected in the vacuum chamber in the absence of plasma. Clearly, both p_n^{div} and p_n^{tmp} increase with $\langle n_e \rangle$, as expected, for all the different plasma vertical positions.

The closer the core plasma is positioned to the baffles, the lower the values of p_n^{div} and p_n^{tmp}, even though the difference between the "medium" and "far" cases is small. The change of

neutral pressure is seen in both p_n^{div} and p_n^{tmp}, thus indicating that this observation is likely not related to the 5 cm movement of the outer strike point, that may affect the neutral trapping. Earlier (in terms of $\langle n_e \rangle$) movements of the CIII front and roll-over of the outer target peak flux (not shown here) are also in agreement with increased p_n^{div} and p_n^{tmp}, as will be discussed in section 3.3.1. The lower p_n^{div} and p_n^{tmp} in the "close" case can be explained by an increased recycling flux on the baffle as discussed in more detail in the following and which results in a lower recycling flux at the outer target. Since the outer leg in the "close" case is closer to the floor baratron gauge than in the other cases and due to the spatial variation of neutral pressure in the divertor [16, 17], the reduction in p_n^{div} may even be underestimated.

The particle flux onto the main plasma facing side of the baffle is obtained from Langmuir probes, figure 1(b). To obtain an estimate of the entire flux onto the baffle the measurements are extrapolated using an exponential fit. We find that the measured integrated flux is approximately 60% of the extrapolated flux in the three cases. In the following, we will therefore extrapolate the measured heat flux to account for fluxes at the baffle tip. The ratio of the integrated ion flux impinging on the outer baffle and of the flux reaching the outer target increases with the proximity of the X-point to the outer baffle (up to 30% in the "close" case), indicating that an increased fraction of the overall recycling occurs on the baffle, figure 4(c). This is consistent with our observations on p_n^{div} and p_n^{tmp}. The heat flux impinging on the outer baffle is evaluated as

$$q_\perp = n_e c_s \left(\gamma T_e + E_{pot}\right) \sin(\alpha) \quad (1)$$

Here c_s is the sound speed, E_{pot} the potential energy carried by the incident ions (E_{pot} = 15.8 eV, following Ref. [29]), γ the sheath heat transmission coefficient (we assume $\gamma = 5$ [19]) and α the grazing angle of the magnetic field. Integrating the extrapolated profiles yields the total power deposited onto the baffle. The ratio of the power into the baffle and the power at the outer divertor target increases with the proximity of the X-point to the outer baffle and reaches 30% in the "close" case, figure 4(d).

The ratios between the integrated particle and heat fluxes, figure 4 (c,d), evolves similarly with the distance of the plasma to the outer baffles. Such an increase of the heat and particle fluxes on the baffles as the plasma is moved closer was simulated using the SolEdge2D-EIRENE2D code, not including drifts [30, 31]. These simulations found that the peak heat flux intercepted by the baffles increases more rapidly than the peak particle flux [31], reaching, in some cases, unacceptable values before optimal gas baffling in terms of neutral compression ratio is reached. To compare these simulations with measurements, we plot in figure 5 the ratios of the peak particles (resp. heat) flux on the baffle and the peak particles (resp. heat) flux on the floor, determined by extrapolation of the Langmuir probes measurements. In the "close" case, both ratios are similar and reach values of up to 30%. In the "medium" case, the values are lower, with peak values of approximately 20%. The simulations, which predicted a higher interception of heat than particle flux interception by the baffles, are, therefore not confirmed in these experiments. The discrepancy could be related to the diffusive treatment of far-SOL transport in the simulations.

The configuration scan shows that the chosen reference equilibrium is close to an optimum for this baffle design in terms of increasing the divertor pressure. This also shows that the optimal baffle length is related to trade-off between the divertor closure and the increase in recycling on the baffles themselves. This was already noted in the simulations in the 2D edge simulations carried out for the design of the gas baffles [10, 31]. Comparing to the simulations results, we find that for the selected baffle design, the optimum closure corresponds to $\rho^{lim}_{\psi,outer} \approx 1.09$ and $\mathrm{dr}^{lim}_{us,outer} = 26.6$ mm, whereas simulations found an optimal closure for, depending on plasma conditions (high-power attached or detached), $\rho^{lim}_{\psi,outer} \approx 1.07$ (resp. $\rho^{lim}_{\psi,outer} \approx 1.043$) and $\mathrm{dr}^{lim}_{us,outer} = 21$ mm (resp. $\mathrm{dr}^{lim}_{us,outer} = 13$ mm) [31]). However, the coarseness of the scans (both in simulations and experiment) introduce a significant uncertainty. We also note that these simulations changed the shape of the baffles instead of moving the plasma. Furthermore, they assumed different plasma current and input power and therefore are not directly comparable to our experiments.

The effect of plasma plugging was also investigated at fixed geometry via a variation in heating power and hence SOL pressure. SOLPS-ITER simulations predicted an increase of the divertor neutral pressure at high $\langle n_e \rangle$ in a case with 1.2 MW of power crossing the separatrix, as compared to a case with only 330 kW. In the experiment the H-mode transition at high heating power limited the range of this L-mode scan to 400kW. At high $\langle n_e \rangle$, a limited scan at lower I_P (190 kA) using additional neutral bream power, for a total input power (Ohmic and beam) ranging from 200 kW to 400 kW hinted at slightly higher neutral pressure in the 400 kW case at high $\langle n_e \rangle$. However, the limited range of the power scan does not allow us to draw a firm conclusion.

3.3. Effect of divertor baffling on detachment physics

In this section, we focus on the effect of the divertor gas baffles on detachment, in the same L-mode reference plasma as discussed in section 3.1. First investigations revealed a reduction of the detachment threshold, as well as access to detachment of the inner target in presence of the baffles [1]. We now extend these results. We first discuss the conditions near the outer and the inner target, before focusing on the evolution of upstream quantities.

3.3.1. Effect on detachment threshold and target profiles

The roll-over of the target ion flux is generally considered as an indicator for the onset of detachment [32]. In all cases, a decrease ("roll-over") of the total ion flux reaching the outer targets, Γ_t^o, occurs at sufficiently high $\langle n_e \rangle$, figure 6(a). In the discharge without baffles, this roll-over is very weak and occurs just at the highest densities reached during the density ramp. A clear roll-over of Γ_t^o can, instead, be seen for the baffled case performed shortly after a boronization, occurring at $\langle n_e \rangle \approx 8.5 \times 10^{19}$ m^{-3}. For the baffled discharge shown in red and magenta, the situation is more complex. This case features

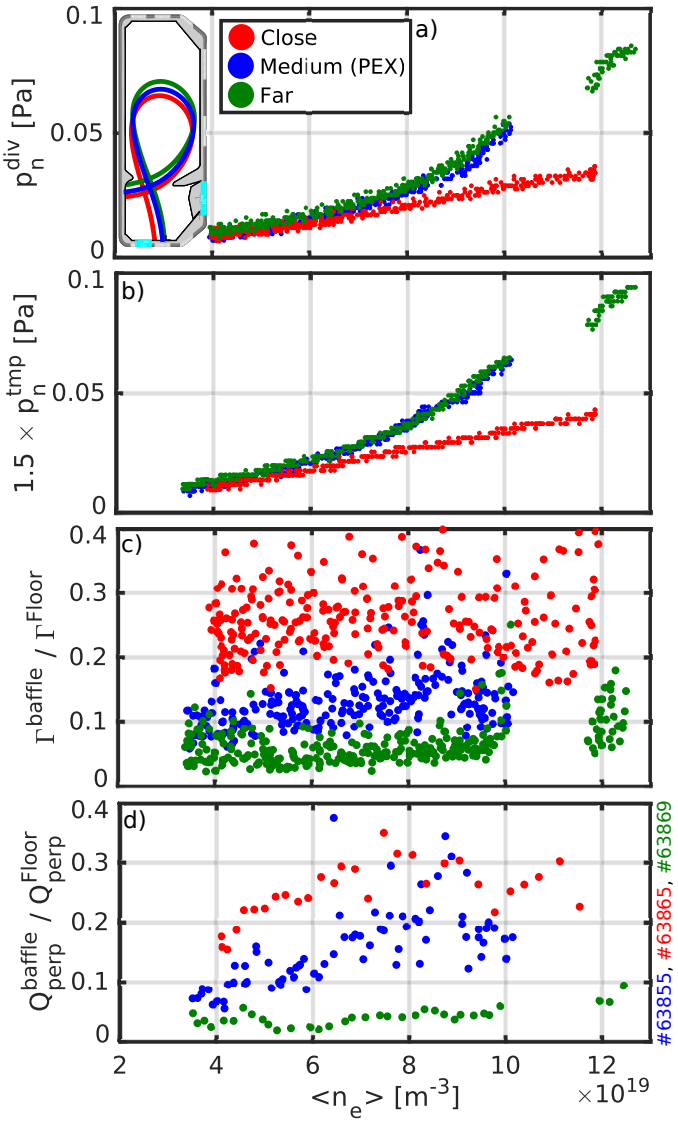

Figure 4: Plasma shapes used to investigate the role of divertor close. The blue shape corresponds to the PEX reference discharge. The red shape is the PEX shape moved towards both baffles. The green shape is the PEX shape moved away from both baffles. The cyan rectangles indicate the positions of the floor and turbo-pump duct baratrons (cf. figure 1) (right panels) (a) Evolution of the divertor neutral pressure for the three cases plotted in the left panel. (b) Evolution of the neutral pressure in the turbo-pomp duct for the three cases plotted in the left panel. (c) Ratio of the (integrated) particle flux reaching the outer baffle to the (integrated) particle flux reaching the outer target. (d) Ratio of the (integrated) heat flux reaching the outer baffle to the (integrated) heat flux reaching the outer target. Due to the absence of Langmuir probes at the tip of the baffles (see figure 1), particle and heat fluxes reaching the outer baffle are exponentially extrapolated.

a BURP, leading to a jump in $\langle n_e \rangle$. The jump in density happens after Γ_t^o reaches a plateau and approximately at the same core density where the discharge without BURP shows the roll-over. Γ_t^o clearly decreases after the jump (as $\langle n_e \rangle$ is further increased), proving that the divertor is then partially detached. We therefore use the "pre-jump" $\langle n_e \rangle$ as an approximate roll-over threshold, at $\langle n_e \rangle = 9 \times 10^{19}$ m^{-3}. This rollover occurs at a slightly higher value of $\langle n_e \rangle$ than in the case close to boronization, but still at lower $\langle n_e \rangle$ than in the case without baffles, which occurs at $\langle n_e \rangle \approx 12 \times 10^{19}$ m^{-3}. The baffles thereby decrease the roll-over threshold by approximately 20-25%. Furthermore, in baffled cases, the reduction in Γ_t^o is substantially larger, indicating a deeper detachment. Note that stronger roll-over is also observed in TCV without baffles, at higher plasma current (320 kA) and at sufficiently large flux expansion [16, 33].

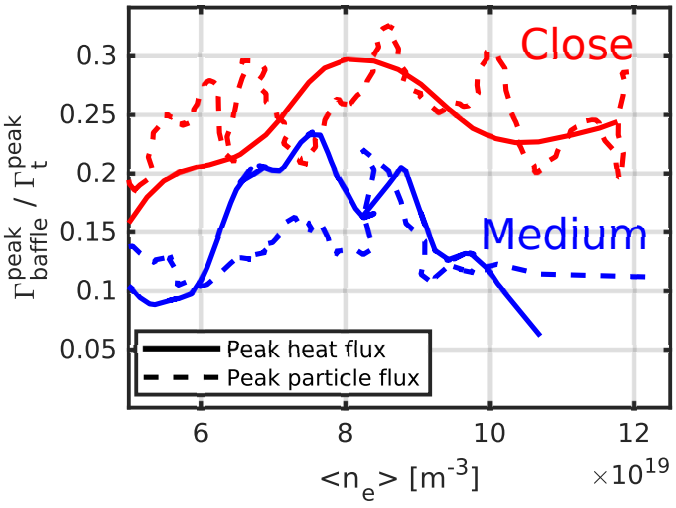

Figure 5: Ratios of the peak particles (resp. heat) flux on the baffle and the peak particles (resp. heat) flux on the floor, as determined by Langmuir probes, for the "close" and the "medium" cases.

To provide a second estimate for the detachment threshold, as done previously on TCV [25, 16, 33], we show in figure 6(b) the behavior of the CIII emissivity front location along the divertor outer leg. In presence of the baffles, the poloidal movement of the CIII front occurs at a lower $\langle n_e \rangle$ than without baffle, indicating a generally lower divertor temperature. Measurements of T_e across the divertor leg using the RDPA confirm this interpretation [34]. Defining a poloidal distance of 15 cm between the CIII front and the X-Point as a definition for a detachment threshold, as done in [35], we find a threshold at $\langle n_e \rangle = 8.2 \times 10^{19}$ m^{-3} for the baffled cases and $\langle n_e \rangle = 11 \times 10^{19}$ m^{-3} for the unbaffled case, compatible with the Langmuir probes (figure 6(a)), thus confirming that the baffles decrease the roll-over threshold by approximately 20%.

Similarly to the divertor neutral pressure as discussed in section 3.1, some variability can be seen in the detachment behavior of nominally equivalent scenarios, as illustrated in figures 6 and 7. In the top panel of figure 7, we plot the detachment $\langle n_e \rangle$-threshold, as determined by the roll-over of Γ_o^t, as well as by CIII front location, as a function of the time since the last boronization, which was identified as one of the factors influencing the discharges. However, no strong correlation can be seen, and both thresholds (Γ_o^t and CIII) generally occur between $\langle n_e \rangle \approx 8 \times 10^{19}$ m^{-3} and $\langle n_e \rangle \approx 10 \times 10^{19}$ m^{-3}. To further assess the shot-to-shot variability as well as the correlation between these two definitions of a detachment threshold, we plot in the lower panel of figure 7 a comparison between these two thresholds, both for baffled and non-baffled shots. It shows a generally good correlation, although there is some scatter, and confirms that, despite some shot-to-shot variability,

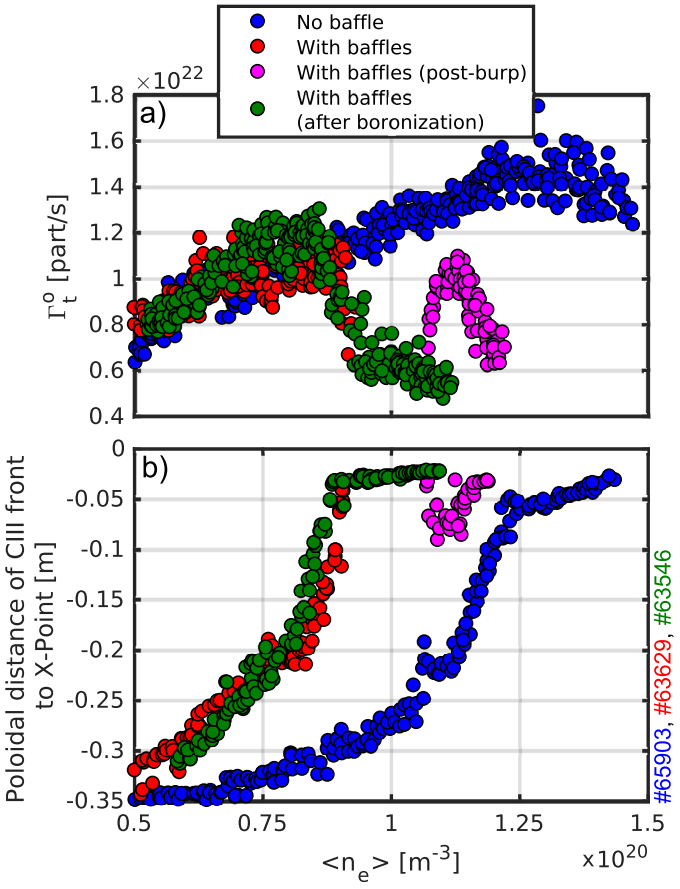

Figure 6: (top) Evolution of the integrated particle flux to the outer target Γ_t^o and (bottom) Poloidal distance between the CIII front and the X-Point as a function of the line-averaged density $\langle n_e \rangle$, in a reference case without baffle (blue), and in two cases with both baffles installed, one of them following a boronization (green).

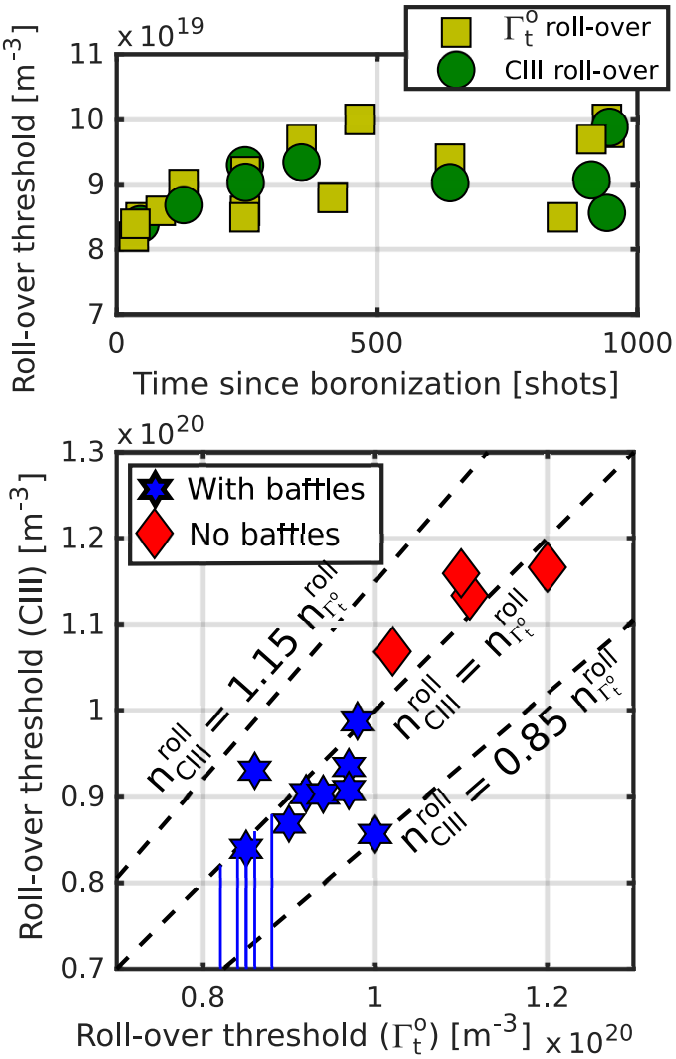

Figure 7: (top) Evolution of the detachment $\langle n_e \rangle$ threshold determined either using the rollover of the outer target ion flux (circles) or the $\langle n_e \rangle$ at which the CIII front is located 15 cm below the X-Point, plotted as a function of shot numbers since the last boronization. (bottom) Detachment threshold as determined by Langmuir probes vs detachment threshold as determined by CIII front location, for baffled and non-baffled shots. The vertical bars indicate the position of the Γ_o^t roll-over for discharges in which MANTIS data were unavailable.

the discharges with baffles generally feature lower detachment threshold.

For more insight on the evolution of target profiles, we now show in figure 8 the outer target electron density and temperatures for the three discussed cases, at two different densities ($\langle n_e \rangle = 7.5 \times 10^{19}$ m^{-3} and $\langle n_e \rangle = 11.5 \times 10^{19}$ m^{-3}). At $\langle n_e \rangle = 7.5 \times 10^{19}$ m^{-3}, i.e. before the roll-over identified in figure 6, we note that cases in presence of the baffles show higher target density and lower target temperature. In particular, the low target temperatures observed with the baffles at any $\langle n_e \rangle$ are compatible with the observations of a early movement of the CIII front towards the X-Point. At higher density ($\langle n_e \rangle = 11.5 \times 10^{19}$ m^{-3}), the target temperature remains smaller in the baffled cases. However, the picture is more complicated for the density. While in the case closely following a boronization, the density shows a sharp decrease compared to its value at $\langle n_e \rangle = 7.5 \times 10^{19}$ m^{-3}, it is not the case in the shot with the BURP, that shows similar target density as at $\langle n_e \rangle = 7.5 \times 10^{19}$ m^{-3}. In the case without baffle, the target electron density keeps increasing as $\langle n_e \rangle$ is increased, even after the roll-over, confirming that the detachment is not very deep. We note, however, that deriving reliable T_e in detached regime (below 5 eV) using Langmuir probes is subject to significant uncertainties [19]. Therefore, for the baffled cases that feature low temperature, the temperature is likely over-estimated and the density under-estimated, as hinted by Stark density measurements from divertor spectroscopy which indicate (line-averaged) values up to 5×10^{19} m^{-3} in chords looking close to the targets [36]. These observations at the outer targets, together with observations of higher divertor neutral pressure, are in agreement with the SOLPS-ITER predictions [17], where the presence of the baffles led to increased ionization source and associated power loss in the divertor. The increase of the ionization source in the divertor in presence has indeed been observed using the RDPA, as will be reported in Ref. [34].

Let us now focus on the behavior of the inner target. In the case without baffle, the total ion flux reaching the inner target,

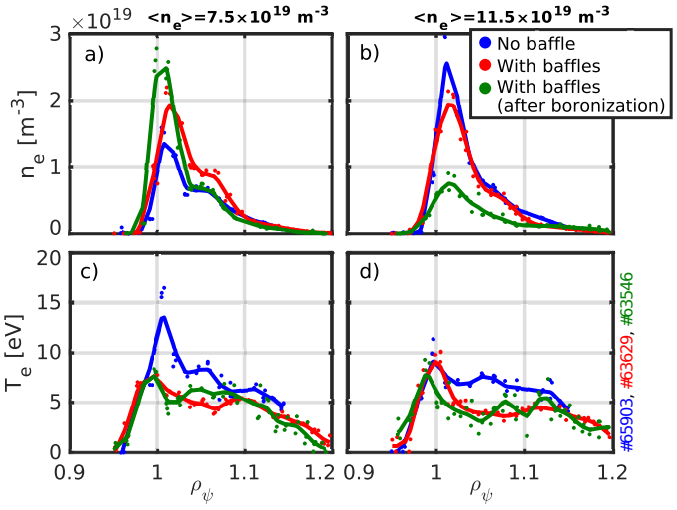

Figure 8: Target profiles of electron density n_e (top row) and electron temperature T_e (bottom row) as a function of ρ_ψ. The left column plots these quantities at $\langle n_e \rangle = 7.5 \times 10^{19}$ m^3, that is, before any roll-over, whereas the right column corresponds to $\langle n_e \rangle = 11.5 \times 10^{19}$ m^3, after the baffled cases roll-overs.

Γ_t^i, increases monotonically with $\langle n_e \rangle$, whereas in cases with baffles, a clear roll-over of Γ_t^i can be seen in both cases, at $\langle n_e \rangle$ matching the roll-over thresholds determined for the outer target, figure 9. This result clearly shows the beneficial role of the baffles to access detachment of the inner target in TCV, in qualitative agreement with predictions by SOLPS-ITER [17] and SolEdge2D-EIRENE [31]. This change of behavior can be ascribed to the presence of the HFS baffle, as will be shown in the next section.

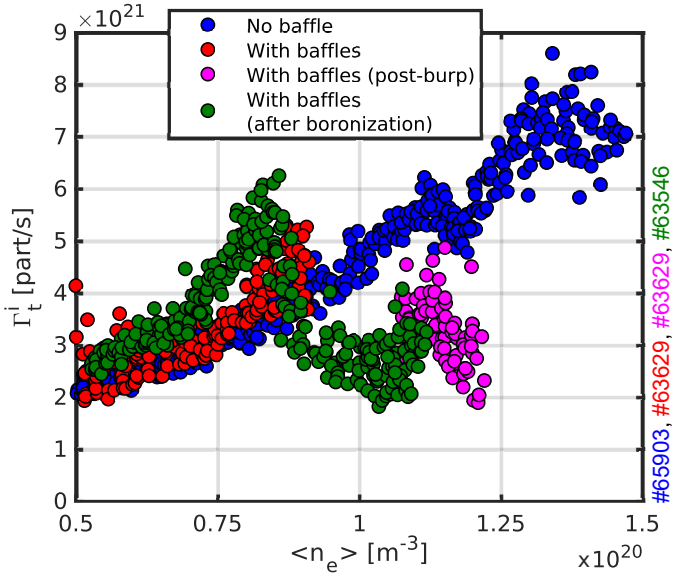

Figure 9: Evolution of the integrated particle flux to the inner target Γ_t^i as a function of the line-averaged density $\langle n_e \rangle$, in a reference case without baffle, and in two cases with both baffles installed.

3.3.2. *Role of inner baffle*

By design, the HFS baffle is relatively short, and thus its impact on the divertor closure can be questioned. To experimentally assess its effect, we plot in figure 10 the particle fluxes and divertor neutral pressure p_n^{div} when the inner divertor leg is positioned either below or above the HFS baffle. As a remark, we note that these two discharges have been done at higher I_P (320 kA). Consistent with the discussion of figure 4, we find that positioning the inner leg above the HFS baffle leads to lower divertor neutral pressure (for a given $\langle n_e \rangle$). Observing now the outer target particle flux Γ_t^o, it appears that changing the position of the inner leg results in a relatively modest increase in the roll-over density. Interestingly, then plotted as a function of divertor pressure rather than $\langle n_e \rangle$, the difference of behavior can be reconciled. The main difference lies in behavior of the inner target. While the inner target particle flux Γ_t^i shows a clear roll-over in the case where the inner leg, at $\langle n_e \rangle = 9 \times 10^{19}$ m^{-3}, is below the HFS baffle, this is not the case in the case where the leg is above the baffle. These observations are consistent with Ref. [1] as well as SolEdge2D-EIRENE [31] simulations, which have shown that in attached conditions, the inner baffle mostly affects the inner divertor.

3.3.3. *Evolution of upstream profiles*

It is well known that divertor detachment can affect the upstream and core plasma. Figure 11 plots profiles of the electron density and temperature measured by the Thomson Scattering (TS) at $\langle n_e \rangle = 11 \times 10^{19}$ m^{-3} for the three cases investigated in section 3.3. All three cases feature similar density profiles, while temperature profiles differ by a range of about 20%. The inserts in figure 11 plot the evolution of the separatrix density n_e^{sep} and temperature T_e^{sep} (with the separatrix position determined by the equilibrium code LIUQE [37]) as a function of $\langle n_e \rangle$ for these tree cases. While for $\langle n_e \rangle < 9 \times 10^{19}$ m^{-3}, all cases have similar behavior, they significantly differ at higher densities. One observes that while at low density, the separatrix density is well fitted by $0.3 \times \langle n_e \rangle$, this is not necessarily the case at higher density. In particular, the case shortly following a boronization shows a large drop of n_e^{sep}, associated to a drop of T_e^{sep}. The other case with baffles only shows a small drop of n_e^{sep}, and no drop of T_e^{sep}. In both cases, this is associated with the formation of a radiation blob (as seen by the bolometry) that lies partially within the confined region, slightly above the X-Point, at the High Field Side. This is currently understood as the onset of a MARFE, that ultimately leads to a disruption. It appears that the earlier (in terms of $\langle n_e \rangle$) the roll-over, the earlier a degradation of the upstream plasma occurs. Therefore, while the baffles reduce the detachment threshold, there is currently no indication that they improve the divertor-core compatibility as the onset of an X-Point MARFE affecting core density also happens at lower $\langle n_e \rangle$.

4. First results in baffled H-mode plasmas on TCV

In TCV, type-I ELMy H-mode plasmas are routinely obtained with NBH, both in conventional and alternative divertor

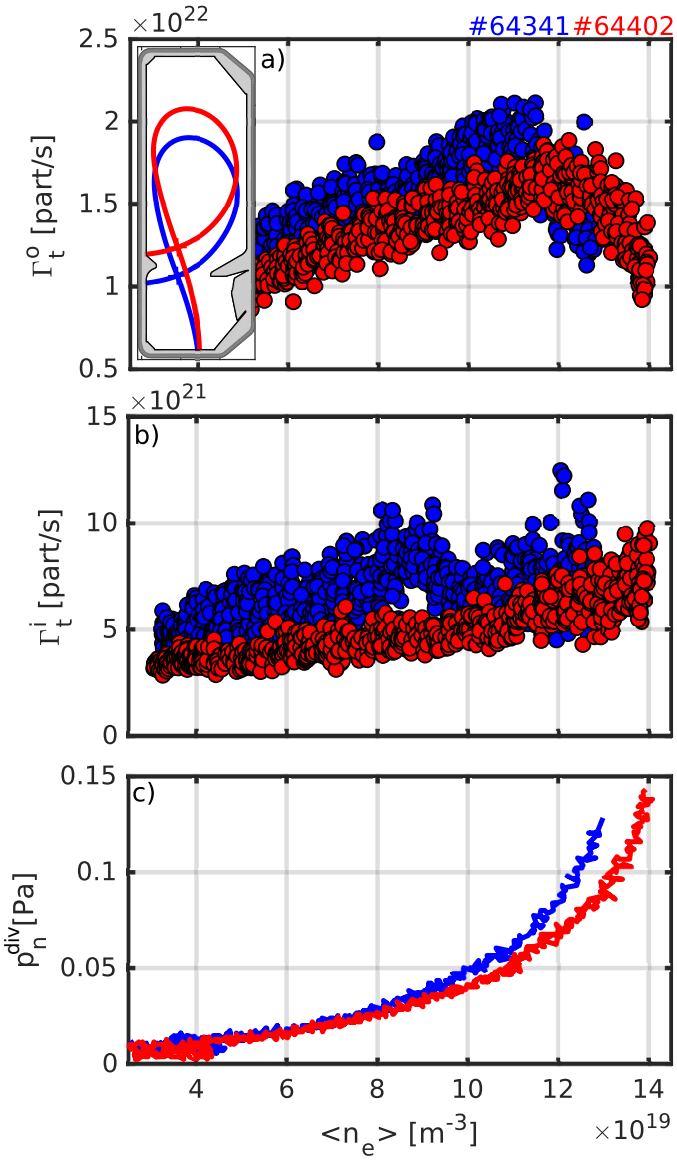

Figure 10: Evolution of the integrated particle flux to the outer target Γ_t^o (top), of the integrated particle flux to the inner target Γ_t^i (middle) and divertor neutral pressure measured by the floor baratron p_n^{div} (bottom) as a function of the line-averaged density $\langle n_e \rangle$ for a case where the inner leg stands below the HFS baffle (blue) and a case where it stands above (red). The insert in the top panel plots the two shapes investigated in this figure.

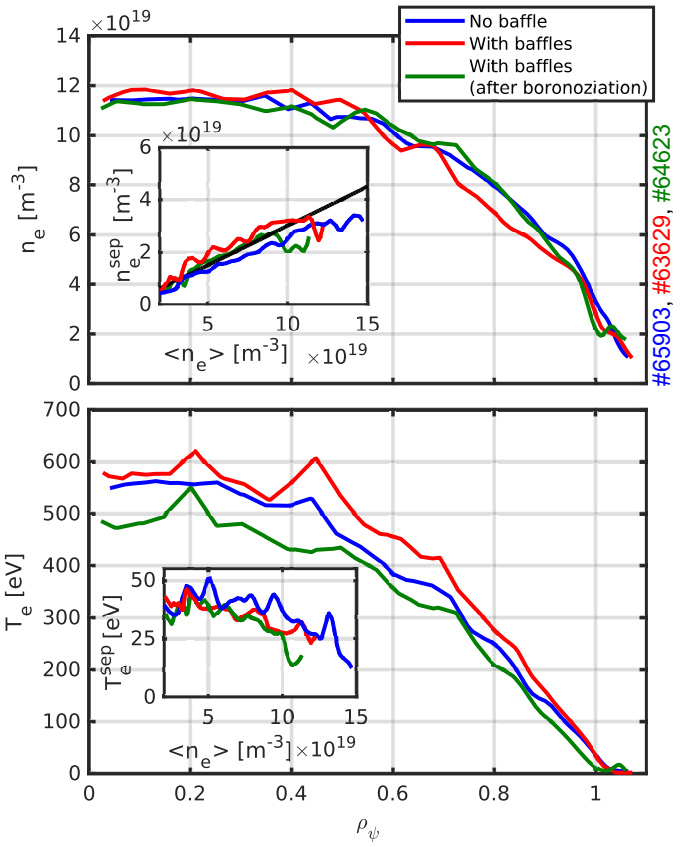

Figure 11: Electron density (top) and temperature (bottom) profiles for $\langle n_e \rangle = 11\times10^{19}$ m^{-3} for the three cases investigated in section 3.3. The inserts plot the evolution of the separatrix density (top) and temperature (bottom) as a function of $\langle n_e \rangle$ for these three cases. In the top insert, the black line corresponds to $0.3\langle n_e \rangle$.

configurations [38]. In these plasmas and without baffles, a reduction of a factor two of the outer divertor power load was achieved using nitrogen (N_2) seeding, together with a reduction of up to 30% of the integrated outer divertor particle flux. To assess the effect of the baffles on H-mode operation, a reference scenario summarized in figure 12 has been developed. It is a Neutral-Beam heated, Lower-Single-Null (LSN) plasma with a plasma current of I_p = 170 kA and with the ion ∇B-drift pointing towards the X-point. Figure 12 plots the main time-traces characterizing these scenarios. In the pre-seeding phase, the ELM frequency is approximately 135 Hz in the baffled case and 150 Hz in the unbaffled case. Both discharges have comparable $\langle n_e \rangle$ (within ±15%), but the radiated power is higher in the baffled case, which is consistent with observations in L-Mode (see section 3.1).

4.1. Observations

Inter-ELM Langmuir probe measurements before N_2 is introduced show low temperature of approximately 6 eV in the unbaffled case, whereas the baffle case show approximately 3 eV. Note that low temperature measurement with Langmuir probes is difficult [19], and the difference between the two cases could be even higher.

In previous studies [25, 16] and in section 3.3.1, it was shown that the poloidal position of the CIII front is a good indicator of the divertor temperature, and can be used to estimate the "closeness to detachment". Figure 13 applies this analysis to the ELMy H-Modes considered here. By detecting peaks of the D_α signal, frames whose exposure time overlapped with ELMs (within a "safety-margin" of 4 ms before and after the ELMs) were removed from the analysis. The data have been binned in 50 ms intervals, and the mean position of the CIII front as well as the standard deviation are shown in figure 13(b)). Let us first comment the case without baffle. At the beginning of the H-Mode phase, without injected N_2, the inter-ELM front location is 20-30 cm away from the X-Point. At the first N_2-seeding level ($\approx 0.5\times10^{20}$ molecules/s), no significant

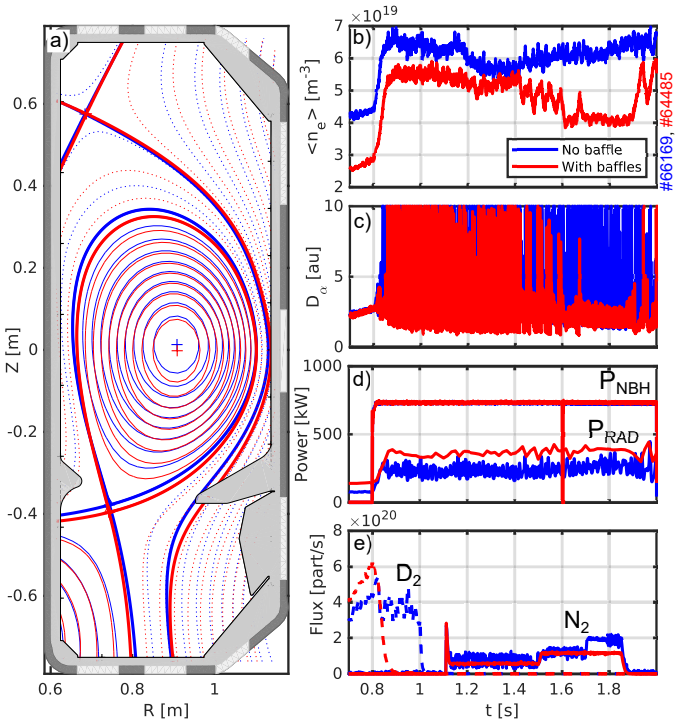

Figure 12: (left panel) Typical shapes of the H-Mode scenarios investigated in this paper. The blue shape corresponds to a discharge performed without the gas baffle, while the red shape corresponds to a discharge done after the installation of the baffles. (right panels) (b) Evolution of the line-averaged density $\langle n_e \rangle$ as a function of time for both the discharge without baffles (blue) and the discharge with baffles (red). (b) Evolution of the D_α signal for both cases. (c). Evolution of the NBH input power P_{NBH} and radiated power P_{rad} in these discharges. (d) Fueling (D_2, dashed lines) and seeding (N_2, solid lines) fluxes for both cases.

change of the CIII front position is seen. It is, however, seen to move towards the X-Point (10-20 cm away) after the second seeding level ($\approx 1 \times 10^{20}$ molecules/s) is reached. Despite a constant seeding level, the front moves progressively towards the X-Point, possibly due to N_2 accumulation in the vessel. As the third seeding level ($2{\times}10^{20}$ molecules/s) is reached, the CIII front reaches close proximity to the X-Point (less than 10 cm). In a similar discharge, it was seen that going to higher seeding level ($\approx 2.3 \times 10^{20}$ molecules/s) led to a loss of H-Mode. At $t = 1.85$ s, the N_2-seeding is stopped, and the CIII-front pulls back away from the X-Point, thus proving that its movement is indeed linked to N_2-seeding. In the case with baffles, the situation is different. At any level of N_2-seeding, or even in the absence of it, the CIII front is close to the X-Point (less than 10 cm away). As N_2 is injected, the scattering of the data points is however decreased, especially at the second seeding level, which could indicate a better buffering of the fluctuations (not the ELMs) that lead to the scatter of the data. At approximately $t = 1.7$ s, this case undergoes a back-transition to L-Mode, and the CIII front stays steadily close the X-Point, without significant fluctuations in its position. After N_2-seeding stops at $t = 1.85$ s, the scenario dithers between L- and H-mode, leading again to a larger further scatter of the position of the CIII front, which remains however close to the X-Point. The baffled discharge clearly features a CIII front closer to the X-Point at any N_2-seeding rates, indicating colder divertor temperatures in H-mode in presence of the baffles.

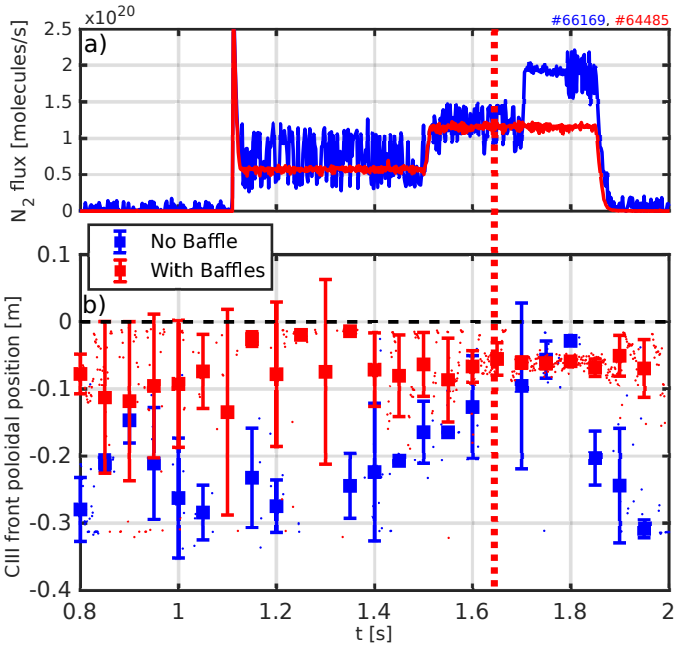

Figure 13: (top) N_2-seeding fluxes in the cases described in figure 12. For an unknown reason, the signal for discharge #66169 is noisy. (bottom) CIII front poloidal position below the X-Point. The points correspond to the raw data, while the squares and errors bars correspond to the mean values and standard deviations of these data points, binned in 50 ms intervals. The vertical dashed-bar indicates the time at which the baffled scenarios exits H-Mode.

Let us now look more closely to the behavior of the CIII front during an ELM and in the inter-ELM period. Figure 14 plots the D_α signal from a photodiode during an ELM and an inter-ELM period, in cases with and without baffles. Five images taken by the MANTIS diagnostic during this period are also plotted. One can see that during the inter-ELM period, the CIII emission along the outer leg is located close to the X-Point in the baffled case, and further away in the case without baffle, as already shown in figure 13. However, during the ELM (fourth picture of panel a, first picture of panel b), in both cases, the inversions show that the CIII radiation is spread along the inner and outer divertor leg, thus indicating that the ELM induced an increase of the divertor leg temperature. Furthermore, the emission peaks at the targets, which can be interpreted as reattachment of the plasma during the ELM, even though the plasma appears to be clearly detached between ELMs.

5. Conclusion

This paper presented experimental results from the TCV divertor upgrade, focusing on the effects of the neutral baffles on the divertor/boundary plasma. The first TCV campaign with a strongly baffled divertor confirmed the key design predictions. A significant increase (factor 2-5) of the divertor neutral pressure has been found with the baffles in a reference L-mode discharge. While the amplitude of the increase is consistent with previous SOLPS-ITER simulations, the absolute

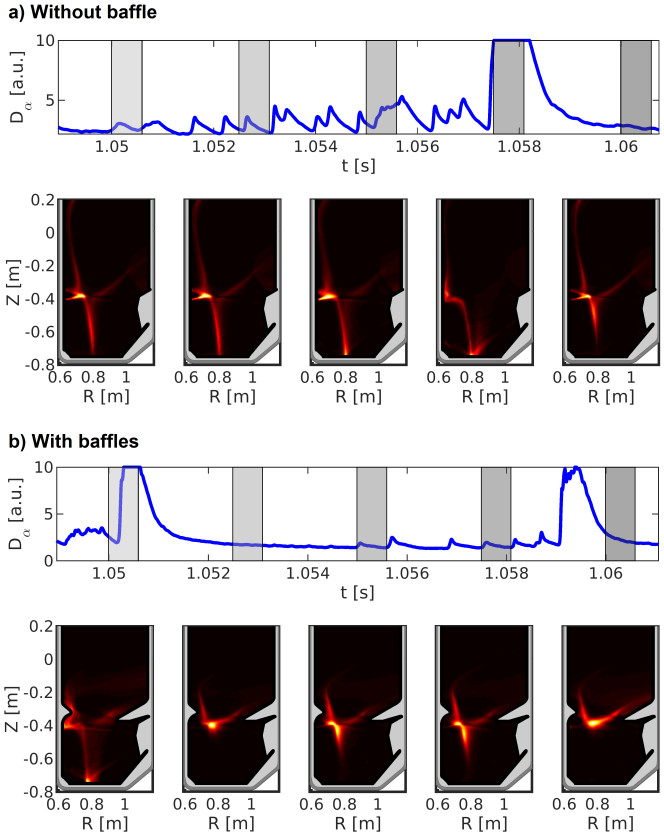

Figure 14: (top) D_α signal from a photodiode, as a function of time. The grey squares indicate the time at which the picture presented in the bottom row are taken, accounting for finite exposure time. (bottom) Images taken by the MANTIS diagnostic (false color) at the times indicated by the vertical dashed lines in the top panel, in chronological order. Panel a) plots a case without baffle while panel b) plots a case with baffles.

amplitude of the divertor neutral pressure is roughly a factor 3-8 lower than in the simulations. The competition between plasma plugging and recycling on the baffles, which was identified in the pre-design SOLPS-ITER simulations and confirmed by SolEdge2D-EIRENE analyses, was also identified in the experiments, which showed that the shape retained to evaluate the impact of the gas baffles on the divertor operation was probably close to the optimum balance between maximizing the plasma plugging while minimizing the recycling on the baffles. In terms of divertor operation, observations in L-Mode at the outer targets indicate a higher divertor density and lower temperature, which is consistent with CIII measurements in the divertor volume, as well as with the increased level of divertor radiation seen by bolometry. The detachment of the outer target is seen to happen at lower $\langle n_e \rangle$ threshold (approximately 20% lower), while the inner target, which generally remained attached in typical TCV $\langle n_e \rangle$-ramps [16, 33] is seen to detach, as a result of the effects of the HFS gas baffle. In H-mode, the access to colder divertor has been facilitated by the baffle, which should also lead to better access to partially detached operation. After a first successful campaign with the gas baffles, they have been removed from the machine for an open divertor campaign. A new set of gas baffle, based on the lessons learnt in the first campaign, is currently being designed and will be installed in TCV in the future.

Acknowledgements

This work was supported in part by the Swiss National Science Foundation. This work has been carried out within the framework of the EUROfusion Consortium and has received funding from the Euratom research and training programme 2014 - 2018 and 2019 - 2020 under grant agreement No 633053. The views and opinions expressed herein do not necessarily reflect those of the European Commission. This work was supported in part by the US Department of Energy under Award Number DE-SC0010529.

References

[1] H. Reimerdes, B. Duval, H. Elaian, A. Fasoli, O. Février, C. Theiler, F. Bagnato, M. Baquero-Ruiz, P. Blanchard, D. Brida, C. Colandrea, H. D. Oliveira, D. Galassi, S. Gorno, S. Henderson, M. Komm, B. Linehan, L. Martinelli, R. Maurizio, J.-M. Moret, A. Perek, H. Raj, U. Sheikh, D. Testa, M. Toussaint, C. Tsui, M. Wensing, the TCV team, the EUROfusion MST1 team, Initial TCV operation with a baffled divertor, Nuclear Fusion 61 (2) (2021) 024002. doi:10.1088/1741-4326/abd196.

[2] T. Eich, A. Leonard, R. Pitts, W. Fundamenski, R. Goldston, T. Gray, A. Herrmann, A. Kirk, A. Kallenbach, O. Kardaun, A. Kukushkin, B. LaBombard, R. Maingi, M. Makowski, A. Scarabosio, B. Sieglin, J. Terry, A. Thornton, A. U. Team, J. E. Contributors, Scaling of the tokamak near the scrape-off layer H-mode power width and implications for ITER, Nuclear Fusion 53 (9) (2013) 093031.

[3] M. Wischmeier, High density operation for reactor-relevant power exhaust, Journal of Nuclear Materials 463 (2015) 22 – 29, plasma-Surface Interactions 21.

[4] H. Reimerdes, R. Ambrosino, P. Innocente, A. Castaldo, P. Chmielewski, G. Di Gironimo, S. Merriman, V. Pericoli-Ridolfini, L. Aho-Mantilla, R. Albanese, et al., Assessment of alternative divertor configurations as an exhaust solution for DEMO, Nuclear Fusion 60 (6) (2020) 066030.

[5] A. W. Leonard, Plasma detachment in divertor tokamaks, Plasma Physics and Controlled Fusion 60 (4) (2018) 044001.

[6] R. Pitts, X. Bonnin, F. Escourbiac, H. Frerichs, J. Gunn, T. Hirai, A. Kukushkin, E. Kaveeva, M. Miller, D. Moulton, V. Rozhansky, I. Senichenkov, E. Sytova, O. Schmitz, P. Stangeby, G. D. Temmerman], I. Veselova, S. Wiesen, Physics basis for the first ITER tungsten divertor, Nuclear Materials and Energy 20 (2019) 100696.

[7] JET Team (prepared by R.D Monk), Recent results from divertor and scrape-off layer studies at JET, Nuclear Fusion 39 (11Y) (1999) 1751–1762. doi:10.1088/0029-5515/39/11y/315.

[8] R. Pitts, R. Chavan, J.-M. Moret, The design of central column protection tiles for the TCV tokamak, Nuclear Fusion 39 (10) (1999) 1433–1449. doi:10.1088/0029-5515/39/10/306.

[9] S. Coda, M. Agostini, R. Albanese, S. Alberti, E. Alessi, S. Allan, J. Allcock, R. Ambrosino, H. Anand, Y. Andrèbe, H. Arnichand, F. Auriemma, J. Ayllon-Guerola, F. Bagnato, J. Ball, M. Baquero-Ruiz, A. Beletskii, M. Bernert, W. Bin, P. Blanchard, T. Blanken, J. Boedo, O. Bogar, T. Bolzonella, F. Bombarda, N. Bonanomi, F. Bouquey, C. Bowman, D. Brida, J. Bucalossi, J. Buermans, H. Bufferand, P. Buratti, G. Calabró, L. Calacci, Y. Camenen, D. Carnevale, F. Carpanese, M. Carr, L. Carraro, A. Casolari, F. Causa, J. Čeřovský, O. Chellaï, P. Chmielewski, D. Choi, N. Christen, G. Ciraolo, L. Cordaro, S. Costea, N. Cruz, A. Czarnecka, A. D. Molin, P. David, J. Decker, H. D. Oliveira, D. Douai, M. Dreval, B. Dudson, M. Dunne, B. Duval, T. Eich, S. Elmore, O. Embréus, B. Esposito, M. Faitsch, M. Farník, A. Fasoli, N. Fedorczak, F. Felici, S. Feng, X. Feng, G. Ferró, O. Février, O. Ficker, A. Fil, M. Fontana, L. Frassinetti, I. Furno, D. Gahle, D. Galassi, K. Galkazka, A. Gallo, C. Galperti, S. Garavaglia, J. Garcia, M. Garcia-Muñoz, A. Garrido, I. Garrido, J. Gath, B. Geiger, G. Giruzzi, M. Gobbin, T. Goodman, G. Gorini, M. Gospodarczyk, G. Granucci, J. Graves, M. Gruca, T. Gyergyek, A. Hakola,

T. Happel, G. Harrer, J. Harrison, E. Havlíčková, J. Hawke, S. Henderson, P. Hennequin, L. Hesslow, D. Hogeweij, J.-P. Hogge, C. Hopf, M. Hoppe, J. Horáček, Z. Huang, A. Hubbard, A. Iantchenko, V. Igochine, P. Innocente, C. I. Schrittwieser, H. Isliker, R. Jacquier, A. Jardin, A. Kappatou, A. Karpushov, P.-V. Kazantzidis, D. Keeling, N. Kirneva, M. Komm, M. Kong, J. Kovacic, N. Krawczyk, O. Kudlacek, T. Kurki-Suonio, R. Kwiatkowski, B. Labit, E. Lazzaro, B. Linehan, B. Lipschultz, X. Llobet, R. Lombroni, V. Loschiavo, T. Lunt, E. Macusova, J. Madsen, E. Maljaars, P. Mantica, M. Maraschek, C. Marchetto, A. Marco, A. Mariani, C. Marini, Y. Martin, F. Matos, R. Maurizio, B. Mavkov, D. Mazon, P. McCarthy, R. McDermott, V. Menkovski, A. Merle, H. Meyer, D. Micheletti, F. Militello, K. Mitosinkova, J. Mlynář, V. Moiseenko, P. M. Cabrera, J. Morales, J.-M. Moret, A. Moro, R. Mumgaard, V. Naulin, R. Nem, F. Nespoli, A. Nielsen, S. Nielsen, M. Nocente, S. Nowak, N. Offeddu, F. Orsitto, R. Paccagnella, A. Palha, G. Papp, A. Pau, R. Pavlichenko, A. Perek, V. P. Ridolfini, F. Pesamosca, V. Piergotti, L. Pigatto, P. Piovesan, C. Piron, V. Plyusnin, E. Poli, L. Porte, G. Pucella, M. Puiatti, T. Pütterich, M. Rabinski, J. J. Rasmussen, T. Ravensbergen, M. Reich, H. Reimerdes, F. Reimold, C. Reux, D. Ricci, P. Ricci, N. Rispoli, J. Rosato, S. Saarelma, M. Salewski, A. Salmi, O. Sauter, M. Scheffer, C. Schlatter, B. Schneider, R. Schrittwieser, S. Sharapov, R. Sheeba, U. Sheikh, R. Shousha, M. Silva, J. Sinha, C. Sozzi, M. Spolaore, L. Stipani, P. Strand, T. Tala, A. T. Biwole, A. Teplukhina, D. Testa, C. Theiler, A. Thornton, G. Tomaž, M. Tomes, M. Tran, C. Tsironis, C. Tsui, J. Urban, M. Valisa, M. Vallar, D. V. Vugt, S. Vartanian, O. Vasilovici, K. Verhaegh, L. Vermare, N. Vianello, E. Viezzer, W. Vijvers, F. Villone, I. Voitsekhovitch, N. Vu, N. Walkden, T. Wauters, M. Weiland, H. Weisen, M. Wensing, M. Wiesenberger, G. Wilkie, M. Wischmeier, K. Wu, M. Yoshida, R. Zagorski, P. Zanca, J. Zebrowski, A. Zisis, M. Z. and, Physics research on the TCV tokamak facility: from conventional to alternative scenarios and beyond, Nuclear Fusion 59 (11) (2019) 112023. doi:10.1088/1741-4326/ab25cb.

[10] A. Fasoli, H. Reimerdes, S. Alberti, M. Baquero-Ruiz, B. Duval, E. Havlikova, A. Karpushov, J.-M. Moret, M. Toussaint, H. Elaian, M. Silva, C. Theiler, D. V. and, TCV heating and divertor upgrades, Nuclear Fusion 60 (1) (2019) 016019. doi:10.1088/1741-4326/ab4c56.

[11] R. Neu, J. Fuchs, A. Kallenbach, C. Maggi, V. Rohde, F. Ryter, T. Eich, J. Gafert, O. Gruber, G. Haas, A. Herrmann, M. Kaufmann, M. Laux, V. Mertens, H. Müller, J. Neuhauser, T. Pütterich, J. Stober, S. Yoon, the ASDEX Upgrade Team, The ASDEX upgrade divertor IIb—a closed divertor for strongly shaped plasmas, Nuclear Fusion 43 (10) (2003) 1191–1196. doi:10.1088/0029-5515/43/10/021.

[12] B. Lipschultz, B. LaBombard, J. L. Terry, C. Boswell, I. H. Hutchinson, Divertor physics research on Alcator C-Mod, Fusion Science and Technology 51 (3) (2007) 369–389. doi:10.13182/FST07-A1428.

[13] G. Fishpool, J. Canik, G. Cunningham, J. Harrison, I. Katramados, A. Kirk, M. Kovari, H. Meyer, R. Scannell, MAST-upgrade divertor facility and assessing performance of long-legged divertors, Journal of Nuclear Materials 438 (2013) S356 – S359, proceedings of the 20th International Conference on Plasma-Surface Interactions in Controlled Fusion Devices.

[14] H. Guo, C. Sang, P. Stangeby, L. Lao, T. Taylor, D. Thomas, Small angle slot divertor concept for long pulse advanced tokamaks, Nuclear Fusion 57 (4) (2017) 044001. doi:10.1088/1741-4326/aa5b46.

[15] H. Guo, H. Wang, J. Watkins, L. Casali, B. Covele, A. Moser, T. Osborne, C. Samuell, M. Shafer, P. Stangeby, D. Thomas, J. Boedo, R. Buttery, R. Groebner, D. Hill, L. Holland, A. Hyatt, A. Jaervinen, A. Kellman, L. Lao, C. Lasnier, A. Leonard, C. Murphy, J. Ren, C. Sang, A. Sontag, T. T. and, First experimental tests of a new small angle slot divertor on DIII-D, Nuclear Fusion 59 (8) (2019) 086054. doi:10.1088/1741-4326/ab26ee.

[16] C. Theiler, B. Lipschultz, J. Harrison, B. Labit, H. Reimerdes, C. Tsui, W. Vijvers, J. A. Boedo, B. Duval, S. Elmore, P. Innocente, U. Kruezi, T. Lunt, R. Maurizio, F. Nespoli, U. Sheikh, A. Thornton, S. van Limpt, K. Verhaegh, N. V. and, Results from recent detachment experiments in alternative divertor configurations on TCV, Nuclear Fusion 57 (7) (2017) 072008. doi:10.1088/1741-4326/aa5fb7.

[17] M. Wensing, B. P. Duval, O. Février, A. Fil, D. Galassi, E. Havlickova, A. Perek, H. Reimerdes, C. Theiler, K. Verhaegh, M. Wischmeier, and, SOLPS-ITER simulations of the TCV divertor upgrade, Plasma Physics and Controlled Fusion 61 (8) (2019) 085029. doi:10.1088/1361-6587/ab2b1f.

[18] M. Wensing, Drift-related transport and plasma-neutralinteraction in the TCV divertor, Ph.D. thesis, École Polytechnique Fédérale de Lausanne, École Polytechnique Fédérale de Lausanne (2021).

[19] O. Février, C. Theiler, H. D. Oliveira, B. Labit, N. Fedorczak, A. Baillod, Analysis of wall-embedded langmuir probe signals in different conditions on the tokamak à configuration variable, Review of Scientific Instruments 89 (5) (2018) 053502. doi:10.1063/1.5022459.

[20] H. De Oliveira, P. Marmillod, C. Theiler, R. Chavan, O. Février, B. Labit, P. Lavanchy, B. Marlétaz, R. A. Pitts, Langmuir probe electronics upgrade on the tokamak à configuration variable, Review of Scientific Instruments 90 (8) (2019) 083502. doi:10.1063/1.5108876.

[21] H. D. Oliveira, C. Theiler, H. Elaian, the TCV team, A fast-reciprocating probe array for two-dimensional measurements in the divertor region of the tokamak à configuration variable, submitted.

[22] W. Vijvers, R. Mumgaard, Y. Andrebe, I. Classen, B. Duval, B. Lipschultz, Conceptual design and proof-of-principle testing of the real-time multispectral imaging system MANTIS, Journal of Instrumentation 12 (12) (2017) C12058–C12058. doi:10.1088/1748-0221/12/12/c12058.

[23] B. L. Linehan, R. T. Mumgaard, M. Wensing, K. Verhaegh, Y. Andrebe, J. R. Harrison, B. P. Duval, C. Theiler, The multi-spectral imaging diagnostic, Review of Scientific Instruments 89 (10) (2018) 103503. doi:10.1063/1.5058224.

[24] A. Perek, W. A. J. Vijvers, Y. Andrebe, I. G. J. Classen, B. P. Duval, C. Galperti, J. R. Harrison, B. L. Linehan, T. Ravensbergen, K. Verhaegh, M. R. de Baar, MANTIS: A real-time quantitative multispectral imaging system for fusion plasmas, Review of Scientific Instruments 90 (12) (2019) 123514. doi:10.1063/1.5115569.

[25] J. Harrison, W. Vijvers, C. Theiler, B. Duval, S. Elmore, B. Labit, B. Lipschultz, S. van Limpt, S. Lisgo, C. Tsui, H. Reimerdes, U. Sheikh, K. Verhaegh, M. Wischmeier, Detachment evolution on the TCV tokamak, Nuclear Materials and Energy 12 (2017) 1071 – 1076, proceedings of the 22nd International Conference on Plasma Surface Interactions 2016, 22nd PSI.

[26] B. Lipschultz, B. LaBombard, E. Marmar, M. Pickrell, J. Terry, R. Watterson, S. Wolfe, Marfe: an edge plasma phenomenon, Nuclear Fusion 24 (8) (1984) 977–988. doi:10.1088/0029-5515/24/8/002.

[27] J. Winter, H. Esser, L. Könen, V. Philipps, H. Reimer, J. Seggern, J. Schlüter, E. Vietzke, F. Waelbroeck, P. Wienhold, T. Banno, D. Ringer, S. Vepřek, Boronization in textor, Journal of Nuclear Materials 162-164 (1989) 713 – 723.

[28] R. Pitts, C. Nieswand, H. Weisen, M. Anton, R. Behn, R. Chavan, M. Dutch, B. Duval, S. Franke, F. Hofmann, B. Joye, J. Lister, X. Llobet, Y. Martin, J.-M. Moret, J. Petrzilka, Z. Pietrzyk, V. Piffl, P. Reinke, M. Rensink, G. Smith, W. [van Toledo], Divertor target profiles and recycling studies in tcv single null lower standard discharges, Journal of Nuclear Materials 241-243 (1997) 867 – 872.

[29] H. Reimerdes, G. P. Canal, B. P. Duval, B. Labit, T. Lunt, W. A. J. Vijvers, S. Coda, G. D. Temmerman, T. W. Morgan, F. Nespoli, B. T. and, Power distribution in the snowflake divertor in TCV, Plasma Physics and Controlled Fusion 55 (12) (2013) 124027. doi:10.1088/0741-3335/55/12/124027.

[30] H. Bufferand, G. Ciraolo, Y. Marandet, J. Bucalossi, P. Ghendrih, J. Gunn, N. Mellet, P. Tamain, R. Leybros, N. Fedorczak, F. Schwander, E. Serre, Numerical modelling for divertor design of the WEST device with a focus on plasma–wall interactions, Nuclear Fusion 55 (5) (2015) 053025. doi:10.1088/0029-5515/55/5/053025.

[31] D. Galassi, H. Reimerdes, C. Theiler, M. Wensing, H. Bufferand, G. Ciraolo, P. Innocente, Y. Marandet, P. Tamain, the EUROfusion MST1 Team, the TCV Team, Numerical investigation of optimal divertor gas baffle closure on TCV, Plasma Physics and Controlled Fusion 62 (11) (2020) 115009. doi:10.1088/1361-6587/abb24f.

[32] A. Loarte, R. Monk, J. Martín-Solís, D. Campbell, A. Chankin, S. Clement, S. Davies, J. Ehrenberg, S. Erents, H. Guo, P. Harbour, L. Horton, L. Ingesson, H. Jäckel, J. Lingertat, C. Lowry, C. Maggi, G. Matthews, K. McCormick, D. O'Brien, R. Reichle, G. Saibene, R. Smith, M. Stamp, D. Stork, G. Vlases, Plasma detachment in JET Mark I divertor experiments, Nuclear Fusion 38 (3) (1998) 331.

[33] O. Février, C. Theiler, J. R. Harrison, C. K. Tsui, K. Verhaegh, C. Wüthrich, J. A. Boedo, H. D. Oliveira, B. P. Duval, B. Labit, B. Lip-

schultz, R. Maurizio, H. Reimerdes, and, Nitrogen-seeded divertor detachment in TCV L-mode plasmas, Plasma Physics and Controlled Fusion 62 (3) (2020) 035017. doi:10.1088/1361-6587/ab6b00.

[34] H. de Oliveira, Particle balance measurements in the divertor volume of TCV using a fast scanning 2D Langmuir probe array, to be submitted.

[35] C. Theiler, A. Thornton, C. Colandrea, H. D. Oliveira, B. Duval, O. Février, A. Fil, D. Galassi, S. Gorno, J. Harrison, B. Labit, B. Linehan, B. Lipschultz, L. Martinelli, R. Maurizio, A. Perek, H. Reimerdes, U. Sheikh, C. Tsui, K. Verhaegh, M. Wensing, the TCV Team, the EUROfusion MST1 Team, Baffled and non-baffled Super-X studies on TCV, in: 3rd IAEA Technical Meeting on Divertor Concepts, 2019.

[36] M. Wensing, L. Martinelli, Private Communication (2020).

[37] J.-M. Moret, B. Duval, H. Le, S. Coda, F. Felici, H. Reimerdes, Tokamak equilibrium reconstruction code liuqe and its real time implementation, Fusion Engineering and Design 91 (Supplement C) (2015) 1 – 15.

[38] J. R. Harrison, C. Theiler, O. Février, H. de Oliviera, R. Maurizio, K. Verhaegh, A. Perek, A. Karpushov, B. Lipschultz, B. P. Duval, X. Feng, S. Henderson, B. Labit, B. Linehan, A. Merle, H. Reimerdes, U. Sheikh, C. K. Tsui, W. A. J. Vijvers, C. Wüthrich, and, Progress toward divertor detachment on TCV within H-mode operating parameters, Plasma Physics and Controlled Fusion 61 (6) (2019) 065024. doi:10.1088/1361-6587/ab140e.